Atomic scale study of polar Lomer–Cottrell and Hirth lock dislocation cores in CdTe

Tadas Paulauskas,[a] Christopher Buurma,[a] Eric Colegrove,[a,b] Brian Stafford,[a] Zhao Guo,[a] Maria K. Y. Chan,[c] Ce Sun,[d] Moon J. Kim,[d] Sivalingam Sivananthan[a] and Robert F. Klie[a]*

[a]Department of Physics, University of Illinois Chicago, Chicago, IL 60607, USA, [b]National Renewable Energy Laboratory, Boulder, CO, USA, [c]Center for Nanoscale Materials, Argonne National Laboratory, Argonne, IL 60439, USA, and [d]Department of Materials Science and Engineering, University of Texas at Dallas, TX, USA. Correspondence e-mail: rfklie@uic.edu

Dislocation cores have long dominated the electronic and optical behaviors of semiconductor devices and detailed atomic characterization is required to further explore their effects. Miniaturization of semiconductor devices to nanometre scale also puts emphasis on a material's mechanical properties to withstand failure due to processing or operational stresses. Sessile junctions of dislocations provide barriers to propagation of mobile dislocations and may lead to work-hardening. The sessile Lomer–Cottrell and Hirth lock dislocations, two stable lowest elastic energy stair-rods, are studied in this paper. More specifically, using atomic resolution high-angle annular dark-field imaging and atomic-column-resolved X-ray spectrum imaging in an aberration-corrected scanning transmission electron microscope, dislocation core structures are examined in zinc-blende CdTe. A procedure is outlined for atomic scale analysis of dislocation junctions which allows determination of their identity with specially tailored Burgers circuits and also formation mechanisms of the polar core structures based on Thompson's tetrahedron adapted to reactions of polar dislocations as they appear in CdTe and other zinc-blende solids. Strain fields associated with the dislocations calculated via geometric phase analysis are found to be diffuse and free of 'hot spots' that reflect compact structures and low elastic energy of the pure-edge stair-rods.

1. Introduction

Many useful and also detrimental properties of solids can be traced back to the underlying structure of dislocations and their behavior. From their roles in crystal growth, to their effects on a material's mechanical, thermal and opto-electronic properties, the technological importance of dislocations can hardly be overstated (Sutton & Balluffi, 1995; Mahajan, 2000). Despite the large amount of theoretical work in this field, experimental knowledge detailing atomically resolved chemical structure of even the most basic dislocation cores has just begun to be accessible. Aberration-corrected scanning transmission electron microscopes coupled with X-ray energy-dispersive (XEDS) or electron energy-loss (EELS) spectrometers can now routinely provide such information (Phillips et al., 2014). Dislocation core structures play a crucial role in determining dislocation mobility and electronic behavior, and are associated with the dislocation regions inaccessible to elasticity theory that otherwise may non-trivially contribute to the total energy. Besides providing a starting point for atomistic first-principles calculations, the study of core geometries can advance the fundamental understanding of dislocation formation mechanisms and their interaction with other defects.

In this paper, we analyze two low elastic energy stair-rod dislocations in the binary II–VI semiconductor CdTe. Because of its nearly ideal direct bandgap ~ 1.5 eV and high absorption coefficient, CdTe is commercially used in thin film photo-voltaics (PVs). The conversion efficiency of CdTe solar cells has seen only minor improvements over the last 20 years despite intense research and development. The current 20.4% laboratory record is still $\sim 10\%$ shy of the theoretical Shockley–Queisser limit (Green et al., 2013; Shockley & Queisser, 1961; National Renewable Energy Laboratory, Best Research-Cell Efficiencies, http://www.nrel.gov/ncpv/images/efficiency_chart.jpg). One of the main challenges in CdTe PVs is increasing the open-circuit voltage (V_{oc}) beyond 900 mV, which is a critical performance metric closely related to electron-hole recombination rates.

Dislocation cores are generally associated with non-radiative recombination centers and it is desirable to better understand their effects on the device performance. Most of the recent theoretical and experimental effort has been focused on investigation of straight dislocations (Li,

Poplawsky *et al.*, 2013; Li, Wu *et al.*, 2013). However, many dislocations in CdTe are seen to be forming more complex structures with the interacting partials often residing on different slip planes. Among them are Lomer–Cottrell (L–C) and Hirth lock dislocations which are analyzed in this paper. Isotropic elasticity theory predicts that it is energetically favorable for two partial dislocations to come together and form the stair-rod dislocations. Even though L–C and Hirth lock are well known textbook examples of stair-rods in face-centered cubic and diamond-cubic-type crystals, their actual core structures, particularly in zinc-blende CdTe, are largely unknown.

Here, we present a chemically resolved atomic configuration of the relatively large L–C core consisting of four atomic columns and extrapolate the chemical composition of two atomic-column-sized Hirth cores. To confirm the identity of the dislocations, we construct Burgers circuits specifically tailored for stair-rods and present their formation mechanisms based on a double Thompson's tetrahedron suited for analyzing polar dislocations.

The analysis of stair-rods is not confined to CdTe, but is equally applicable to other binary zinc-blende and also elemental solids with diamond-cubic structure. All these solids are tetrahedrally coordinated with the dominant slip system $\{111\}\langle110\rangle$ (Hornstra, 1958; Nunes *et al.*, 2004). In this group, two possibilities exist for motion of dislocations. The slip could occur by breaking a single bond per atom in the shuffle set or three bonds per atom in the glide set. In the following we will only be concerned with the glide set which, due to the ease of a dislocation's dissociation into partials, is generally taken as the primary means of slip (Louchet & Thibault-Desseaux, 1987). This assumption in CdTe is supported partly by the fact that dislocations are mainly observed in their dissociated form and that the stacking-fault energy (9 ± 1 mJ m^{-2}) is also rather low (Takeuchi & Suzuki, 1999).

Unlike elemental diamond-cubic, zinc-blende materials are non-centrosymmetric and exhibit crystallographic polarity. In the present discussion, this means that the cores of straight dislocations can terminate either with Cd or Te atomic columns (metal and non-metal type or *a*- and *b*-dislocations by convention, respectively) and different combinations must be taken into account when considering cores of intersecting dislocations. In addition, zinc-blende crystals have partially ionic bonding character which increases going from III–V to II–VI compounds (Takeuchi & Suzuki, 1999). Hence the electrostatic interaction of core atoms may be a significant factor in addition to the elastic terms to gauge whether a particular reaction is energetically favorable. Studies show that in dislocation core reconstruction of 30° Shockley partials in covalent diamond structures, as well as in III–V GaAs, dimers form along the line further reducing the total energy of the dissociated dislocations (Blumenau *et al.*, 2003; Beckman *et al.*, 2002). In CdTe, the Cd–Cd and Te–Te dimers were shown to be only weakly interacting and it is likely that at finite temperatures the cores still possess a number of dangling bonds (Li, Wu *et al.*, 2013). Atomic configurations of L–C and Hirth lock dislocation cores, which can be taken to form by

two intersecting polar 30° partials, provide a first glimpse into whether they are electrically active, and if so, how they could be passivated.

The stair-rod dislocations, discussed here, are pure-edge dislocations and thus could potentially be found in low-angle tilt-grain boundaries. In fact, identical Cd- or Te-rich L–C-like core arrangements form a subset of structural units found in CdTe coincidence site lattice (CSL) $\{112\}$ $\Sigma3$ and $\{114\}$ $\Sigma9$ grain boundaries (Li *et al.*, 2014; Yan *et al.*, 2003). Miniaturization of semiconductor devices to nanometre scale and fabrication of nanostructures require taking into account a material's plasticity and deformation mechanisms to prevent mechanical failure. Stair-rod dislocations, due to their sessile nature, can cause dislocation pile-ups and thus could play an important role in a material's response to external stresses. The present study of dislocation cores and formation of polar stair-rods concerns many relevant semiconductor crystal structures where the electronic and mechanical properties of a device are under consideration.

2. Experimental methods

Polycrystalline CdTe thin films used in our study were incorporated in the typical CdS/CdTe on a glass superstrate solar-cell structure (Colegrove *et al.*, 2012). The CdTe layer, approximately 10 μm thick, was grown by close space sublimation (CSS) in a helium and oxygen environment on top of a chemical bath deposited (CBD) oxygenated CdS layer. The CdTe layer from the resulting deposition contains randomly oriented grains with an average diameter of about 1 μm. The post-deposition CdCl$_2$ annealing process, commonly used in commercial poly-CdTe-based solar cells, was not performed on these samples. Chlorine introduced in this process tends to segregate at grain boundaries and intra-grain dislocation cores and is thus unwanted in this particular study of native CdTe defects. Cross-sectional TEM (transmission electron microscopy) samples were prepared from the as-grown samples using the focused ion beam (FIB) method.

Atomic resolution *Z*-contrast images and XEDS mappings were collected with a probe spherical aberration corrected JEOL JEM ARM-200CF scanning transmission electron microscope operated at 200 keV beam energy. The microscope is equipped with a cold-field emission gun and can achieve better than 80 pm spatial resolution under optimal operating conditions. The *Z*-contrast images were acquired using a high-angle annular dark-field (HAADF) detector spanning 54–220 mrad semi-angle range. The probe convergence semi-angle was set to 28 mrad, resulting in a probe size of approximately 78 pm and a probe current of 19 pA. The pixel sizes of the HAADF images are ~0.13–0.16 Å. A windowless XEDS silicon drift detector X-Max^N 100 TLE from Oxford Instruments was used to collect atomic-column-resolved X-ray spectrum images from the L–C dislocation core. Here, XEDS mapping is preferred over EELS chemical mapping, which uses Cd *M* and Te *M* edges that suffer from poor signal-to-noise ratio due to the delayed edge onsets. The Cd *L* and Te *L* peaks were used for the X-ray maps with

sample drift correction applied within the Oxford Instruments *AZtec* software. To obtain more signal the probe size was increased to 1.3 Å, which provides approximately 140 pA of probe current at the same probe convergence angle. The pixel size of the raw X-ray spectrum image is approximately 0.27 × 0.27 Å. We used 250 µs pixel dwell time and applied 2× binning and 3 pixel by 3 pixel smoothing to the raw image. It took approximately 70 full frames and less than 5 min to obtain each X-ray map shown in this paper. The local sample thickness was measured to be ∼30 nm using the EELS log-ratio method (Egerton, 1996). No noticeable damage, alterations or material loss were observed during data acquisition from the dislocation cores discussed here.

The geometrical phase analysis (GPA) method was employed to investigate dislocation strain fields from the experimental HAADF images (Hÿtch *et al.*, 1998). The
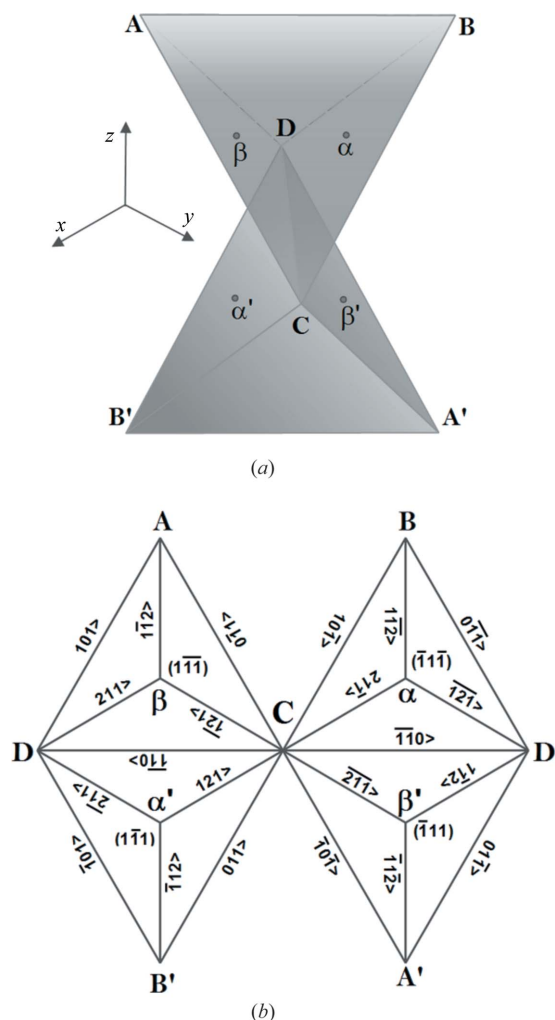

(*a*)

(*b*)

Figure 1
(*a*) Construct of two Thompson's tetrahedra connected along the common edge **CD**. The upper tetrahedron is used for labeling *b*-type dislocations while the lower is for *a*-type. Only glide planes *BB′CD* and *AA′CD* are considered here for dislocation reactions. (*b*) Unfolded representation of planes *AA′CD* and *BB′CD* with indices labeling positive Burgers vectors' directions of perfect and partial dislocations. Miller indices of the two {111} lattice planes refer to their outward normal vectors.

formalism is implemented within Gatan Digital Micrograph software using *FRWRtools* (C. T. Koch, http://elim.physik.uni-ulm.de). Symmetric strain tensor components ε_{xx}, ε_{yy}, ε_{xy} and rigid-body rotation ω_{xy} are calculated with respect to a reference area sufficiently far away from any defects. Two non-collinear reciprocal-lattice vectors (Bragg reflections) of the form $\langle 111 \rangle^*$ are chosen to define a reference lattice. The reciprocal-space apertures used for GPA measurements correspond to a 1.5 nm spatial resolution, which provides a good compromise between noise levels and accuracy desired in this work.

3. Theoretical setup

Thompson's tetrahedron construction is used here to help visualize and keep track of Burgers vectors (Thompson, 1953; Hirth & Lothe, 1982). In CdTe, the faces of the tetrahedron correspond to glide planes that separate Cd and Te terminated {111} planes. However, when discussing polar Hirth and L–C stair-rods, it is cleaner to use two Thompson's tetrahedra joined along a single edge. Fig. 1(*a*) shows a construct of two such tetrahedra joined along **CD**. The top tetrahedron is used solely for labeling *b*-type dislocations and the bottom for *a*-type. We follow the Start-to-Finish/Right-Hand (SF/RH) convention for defining local Burgers vectors and the formal treatment where all operations (including association of intrinsic/extrinsic stacking faults to partials) are to be carried out as viewed by an observer outside the tetrahedron. Looking towards a particular glide plane where a slip is taking place, all the atoms on the opposite side of the separating glide plane will move relative to all the atoms on the observer's side in the direction of one of the Burgers vectors. Thus, slip takes place on the 'inside' of a tetrahedron. It is noted that the inner faces of *ABCD* are all terminated with Te atoms, while all the inner faces of *A′B′CD* terminate with Cd. For the present discussion, we only need to consider dislocations on *AA′CD* and *BB′CD* glide planes.

To simplify reading of the Burgers vectors, we flatten the geometrical figure. This unfolding is done by cutting the *AD*, *BD*, *A′D*, *B′D* and *CD* edges. The two-dimensional representation in Fig. 1(*b*) is then obtained by discarding planes *ABC*, *ABD*, *A′B′C*, *A′B′D* and rejoining the remaining two pairs of planes along *CD*. Miller indices of the planes in Fig. 1(*b*) are labeled according to their outwards normal vectors. Crystallographic directions of perfect and partial positive Burgers vectors are enumerated such that the vectors on the two lower planes *A′CD* and *B′CD* refer to the glide of *a*-type dislocations, while those of the upper, *ACD* and *BCD*, refer to *b*-type. The negative of 30° or 90° partial dislocations' Burgers vectors of either type can in principle be used to associate extrinsic stacking faults.

It should be noted that in a *Z*-contrast image, viewing our crystal along a $\langle 110 \rangle$ direction, we see two sets of {111} planes edge-on. Hence, the vectors that we obtain from the images are only the edge components of an actual Burgers vector. However, knowing the edge component is sufficient to determine the type of a partial or perfect dislocation that we

are looking at, up to the sign of its screw component. STEM (scanning transmission electron microscopy) imaging of pure screw dislocations is in general more challenging, since the atom displacements are parallel to the microscope optical axis. However, it has recently been demonstrated that depth sectioning and exploitation of the crystal surface relaxations (Eshelby twist) can be used to obtain HAADF image contrast from end-on screw dislocations (Cosgriff *et al.*, 2010).

4. Lomer–Cottrell dislocation

An experimental HAADF image and an atomic-column-resolved XEDS map of an L–C dislocation along the [$\bar{1}10$]

zone-axis are presented in Fig. 2(*a*). More specifically, two intrinsic stacking faults are seen in the HAADF image and the XEDS spectrum image shows the integrated intensity of the Cd and Te *L* peaks in the defective lattice region. The dislocation core, which we assume is not jogged, is located at the vertex of two intersecting stacking faults, and is composed of three Cd atomic columns and a single Te column (Cd_3Te), as can be seen from the spectrum image map shown in Fig. 2(*a*).

The chemical composition of the core columns could in principle also be inferred based on the variation of image intensity associated with the atomic dumbbells, since Te columns ($Z = 52$) appear brighter than those of Cd ($Z = 48$), despite the small difference in their atomic numbers (the
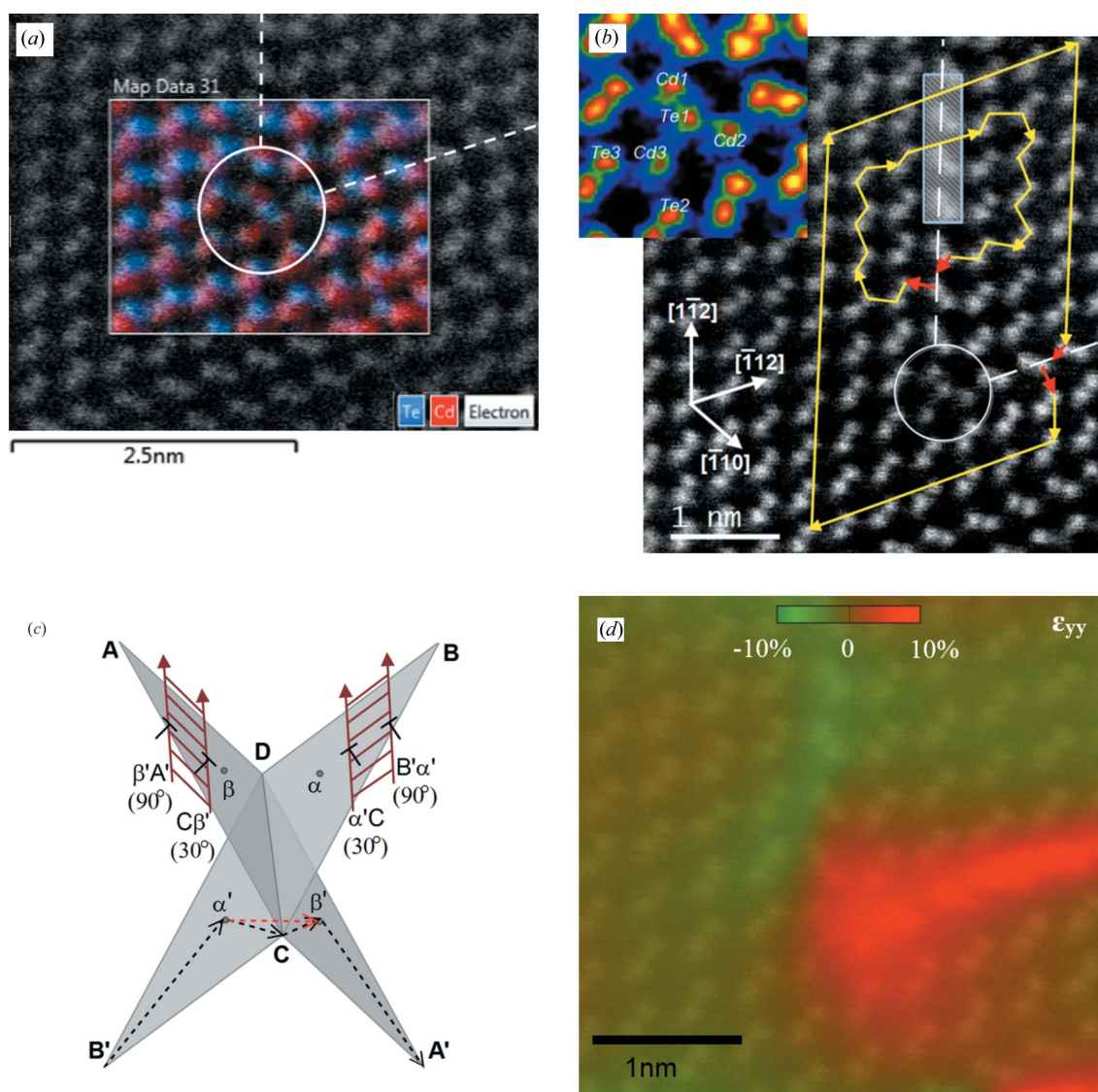
Figure 2
(*a*) Atomic-column-resolved XEDS map overlaid on top of the *Z*-contrast image in the ⟨110⟩ projection. L–C dislocation core (circled) is associated with the two dashed intrinsic stacking faults. (*b*) Illustration of the two SF/RH Burgers circuits and the 'unfaulted' gap (dashed box) in the crystal. The smaller circuit is drawn indicating all the atom-to-atom steps while the larger one omits the middle steps for simplicity. Small red arrows correspond to the first and last steps, while the temperature-contrast coded inset shows the atom labels for reference to the interatomic distances. (*c*) The initial arrangements of the pair of partial dislocations with their associated edge components (tilted T) bounding intrinsic stacking faults (dashed). Burgers vectors are labeled according to the lower tetrahedron, which corresponds to *a*-type (Cd core) dislocations. The red arrow indicates the resulting Burgers vector $\alpha'\beta'$ of L–C dislocation after reaction of the 30° partials along **CD**. (*d*) GPA map of the L–C dislocation compression/tension tensor component in the vertical direction of the image plane. The color scale shows the range −10% to 10% of local lattice strains.

contrast scales as $\sim Z^2$). The contrast of atomic columns at dislocation cores can be affected by dynamical scattering effects due to lattice strain, as well as any possible point defects. Hence, extrapolation could be used to make a first guess of the composition. Such a method has been successfully applied in the recent study of CdTe presenting many different types of straight dislocations that can be found in this material (Li, Poplawsky *et al.*, 2013).
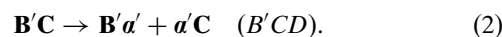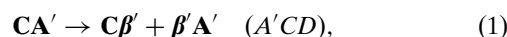
4.1. Verification of the Burgers vector

In order to confirm that this is indeed an L–C core we proceed to determine the Burgers vector in Fig. 2(*b*). Two Burgers circuits are needed in this case since the faulted material can only be crossed once in a single loop. Following the prescription given by A. H. Cottrell, we start by giving one of the stacking faults an internal boundary inside which the material is assumed to be unfaulted (Cottrell, 1965). The boundaries terminate with partial dislocations since the faults end within good material. Next, we construct two SF/RH circuits as shown in the image, starting and ending on the respective faulted planes and passing through the unfaulted gap in the crystal (Cottrell, 1965; Kovacs & Zsoldos, 1973). The local Burgers circuits in CdTe can be constructed by taking two types of atom-to-atom steps: connecting Cd and Te atoms within each dumbbell and by connecting Cd and Te atoms on the adjacent dumbbells along the route. The step through the dumbbell in the unfaulted gap is in the same direction as the corresponding steps within the good material. The Burgers vectors for each of the two circuits are found to lie within the respective faulted {111} planes. The two vectors point away from the vertex along the directions [1$\bar{1}$2] and [$\bar{1}$12], respectively. Their magnitudes correspond to 30° Shockley partials edge components, which are of the form $a/12\langle112\rangle$, where a is the CdTe lattice parameter. Finally, by subtracting the Burgers vector of the smaller circuit from that of the larger one, the Burgers vector of the stair-rod dislocation is found correctly as $a/6[\bar{1}10]$. This subtraction isolates the Burgers vector of the stair-rod since, by construction, the large circuit also encloses a partial dislocation which terminates the stacking fault at the boundary of the unfaulted gap. A similar procedure is also used to find the Burgers vector of single partial dislocations in a stepped extrinsic stacking fault configuration (Kovacs & Zsoldos, 1973). We note that there is still an ambiguity with respect to assigning the 'unfaulted' region to a particular stacking fault and ordering of the circuits within an image. However, the difference in interchanging them shows up as an overall ± sign in a final Burgers vector and thus corresponds to polar variants of a stair-rod dislocation. Thus, information about the chemical composition is needed to correlate with the ordering, which can be obtained either directly *via* HAADF imaging or EELS/XEDS spectroscopies as discussed above.
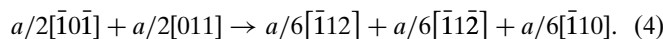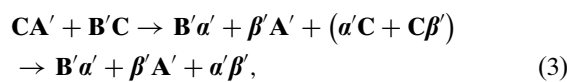
4.2. Discussion of Lomer–Cottrell dislocation formation

Cores of L–C dislocations can have two different chemical compositions because of the polar structure of CdTe. Besides Cd$_3$Te, the second variant has three Te atomic columns and a single Cd column at the center (Te$_3$Cd). We now outline a scenario which leads to the formation of the Cd-rich L–C core. We start with a reference state of two isolated *a*-type perfect 60° dislocations (CA′ and B′C) on different {111} planes and let them dissociate into 30° (Cβ′ and α′C) and 90° (β′A′ and B′α′) Shockley partial dislocations according to equations (1) and (2), which refer to Fig. 2(*c*). The partials, therefore, are of *a*-type as well.

$$\mathbf{CA'} \rightarrow \mathbf{C\beta'} + \boldsymbol{\beta'}\mathbf{A'} \quad (A'CD), \tag{1}$$

$$\mathbf{B'C} \rightarrow \mathbf{B'\alpha'} + \boldsymbol{\alpha'}\mathbf{C} \quad (B'CD). \tag{2}$$

The initial arrangements of the pair of 30° and 90° partial dislocations bounding intrinsic stacking faults are also graphically shown in Fig. 2(*c*). Positive dislocation lines and the imaging zone axis are both chosen to be along **CD** and the order of partials is determined according to an observer outside the tetrahedron. We next assume that applied shear stresses drive both leading 30° partials towards **CD** close enough for the elastically attractive reaction in equation (3) to proceed. Equation (4) depicts the same process (guided by the conservation of the total Burgers vector), in terms of the reactant and final product Burgers vectors crystallographic directions, as labeled in Fig. 1(*a*).

$$\mathbf{CA'} + \mathbf{B'C} \rightarrow \mathbf{B'\alpha'} + \boldsymbol{\beta'}\mathbf{A'} + (\boldsymbol{\alpha'}\mathbf{C} + \mathbf{C\beta'})$$
$$\rightarrow \mathbf{B'\alpha'} + \boldsymbol{\beta'}\mathbf{A'} + \boldsymbol{\alpha'\beta'}, \tag{3}$$

$$a/2[\bar{1}0\bar{1}] + a/2[011] \rightarrow a/6[\bar{1}12] + a/6[\bar{1}1\bar{2}] + a/6[\bar{1}10]. \tag{4}$$

The reaction is elastically favorable because the two 30° partial dislocations have opposite screw components which cancel each other, leaving the product a pure-edge L–C dislocation. To show formation of the Te$_3$Cd L–C core, one could start with two dissociated *b*-type 60° perfect dislocations with Burgers vectors assigned based on the upper tetrahedron. Intersection of the respective *b*-type 30° partials along **CD** (*i.e.* αC + Cβ) then leads to the Te-rich L–C core. The meeting of two *a*-(*b*)-type 30° partials in an otherwise perfect crystal already suggests that the L–C core will be two Cd(Te) cores in excess.
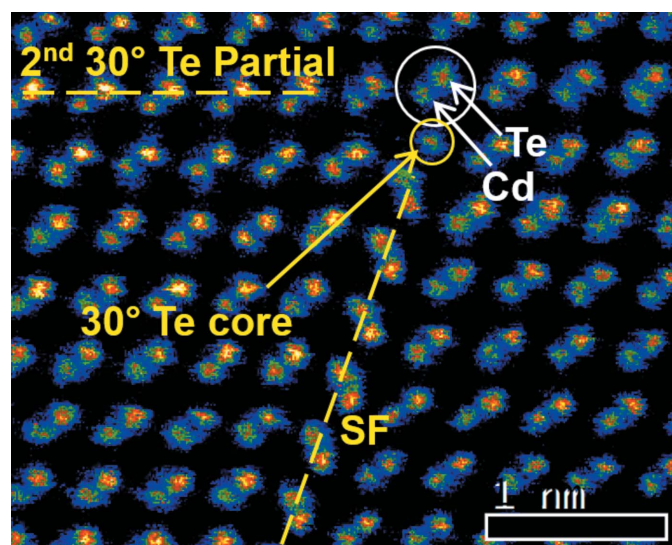
This process could be more easily visualized by referring to the HAADF image in Fig. 3 of a single 30° partial (*b*-type in this case). The dashed line on the other {111} plane is assumed to be the position of the second *b*-type 30° partial. The single Te–Cd dumbbell at the intersection of two approaching partials inevitably takes part in the reaction which qualitatively suggests the four-atomic-column final Te$_3$Cd core configuration. It is likely that there is more than one metastable arrangement of the intra-core atoms. Indeed, we experimentally observed an L–C core where the middle column is drawn upwards so that the full dumbbell at the vertex is still seemingly intact. It is worth noting that L–C dislocations can also form by dissociation of a Frank partial and by a Fleischer cross-slip of a partial dislocation (Hirth & Lothe, 1982). The different atomic pathways could possibly lead to slight variations of the L–C core.

Additional information can be gained about the core by examining the projected atom-to-atom distances from the inset of Fig. 2(b). The distances are obtained by measuring peak-to-peak separations in atom-width integrated line contrast profiles of the Z-contrast images. No significant residual sample drift was observed during the acquisition times and the main uncertainty in the measured distances is due to the pixel size (± 0.16 Å). The values may also be affected by lattice strain associated with several other defects in the vicinity. The measured distances Cd3—Te1, Cd3—Te2 and Cd3—Te3 are 2.78, 2.81 and 2.92 Å, respectively, values which are very close to the experimental bond length 2.805 Å. The angles Te2—Cd3—Te3, Te1—Cd3—Te3 and Te2—Cd3—Te1 are 120, 130 and 110°, respectively ($\pm 4°$). This suggests that the three bonds are nearly planar within the image plane and Cd3 is close to the sp^2 configuration. It can be noted that the Cd3 column has an almost identical first nearest neighbor's environment as an isolated 30° partial. Based on the distances Te1 is likely to be over-coordinated with five nearest Cd columns.

4.3. Strain-field analysis

The strain tensor component $\varepsilon_{yy}(\mathbf{r})$ of the L–C dislocation, calculated via GPA, is shown in Fig. 2(d). It illustrates the local lattice tension/compression in the vertical direction of the image plane. From the strain map we see that most of the distortions are associated with the stacking faults and confined to no more than a single {111} lattice plane. A small diffuse region in tension on the inner side of the core can be identified, although its extension downwards could be traced to another dislocation three lattice planes below. Shear stress $\varepsilon_{xy}(\mathbf{r})$ and also $\varepsilon_{xx}(\mathbf{r})$, $\omega_{xy}(\mathbf{r})$ of the L–C dislocation, not presented here, are likewise localized to the stacking fault

planes. Strain mapping of features at and below unit-cell dimensions tends to break down in GPA and may introduce large errors (Hÿtch & Plamann, 2001). The narrow stacking fault defect is of this size and the calculated strain values at the interface may not be reliable. Furthermore, the well known 'fly back' error in STEM GPA calculations produces artifacts parallel to the fast scan direction. We observed strain variations up to $\pm 3\%$ due to this effect (Zhu et al., 2013). Nevertheless, the accuracy of our analysis is sufficient for the qualitative investigation of strain distributions in the lattice surrounding the L–C core. Namely, we note that no 'hot spots' are present in the stair-rod configuration, as is usually seen in pure-edge dislocations, which tend to have the characteristic dipole-shaped fields. The absence of such features reflects highly reduced lattice distortions of the extended L–C dislocation.
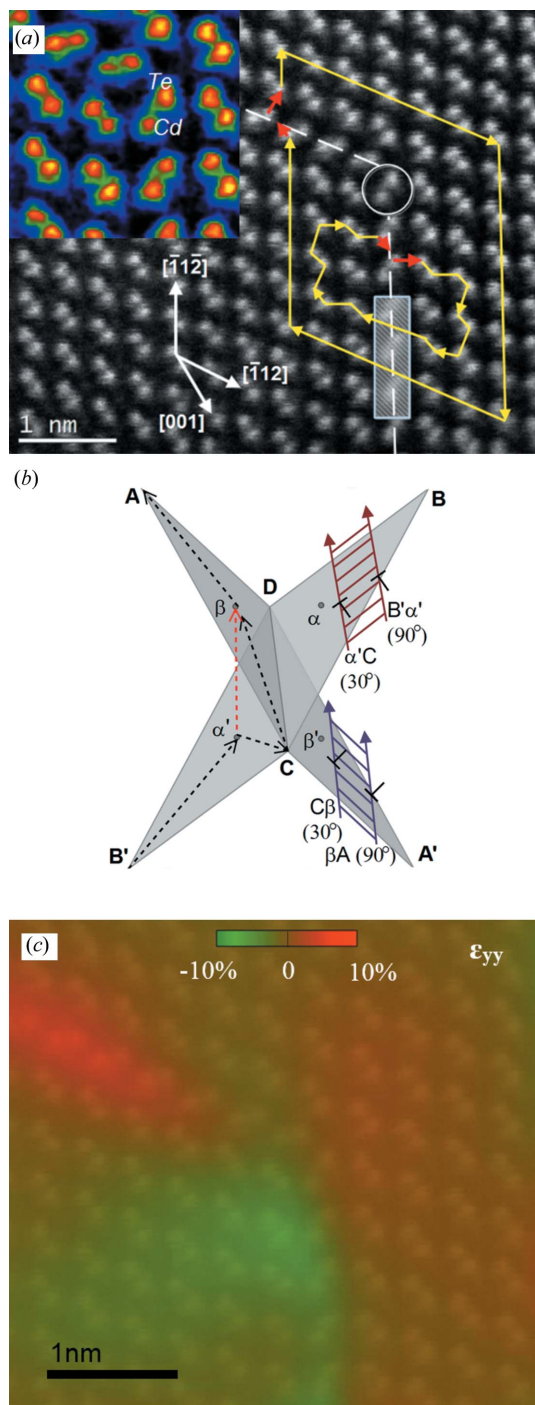
5. Hirth lock

Next, we discuss the Hirth lock dislocation core, which is another elastically stable, obtuse stair-rod dislocation (Fig. 4a). The HAADF image clearly shows that the dislocation core at the vertex of two intrinsic stacking faults consists of one Cd and one Te atomic column. The intra-core atoms seem to form a new dumbbell structure and it is likely that all four Cd—Te bonds are satisfied. In the $\langle 110 \rangle$ projection their interatomic distance of 1.91 Å is, however, 15 $\pm 5\%$ elongated compared to the perfect dumbbell, where two bonds are held. The chemical composition of this core is extrapolated based on variations in the HAADF image contrast of the surrounding atoms (Li, Poplawsky et al., 2013). The proposed composition is further supported by the lack of local atomic-column distortions that would likely be associated with the same kind of partially ionic bonded atomic species, as well as the formation mechanism, discussed below, which agrees with the core arrangement.

5.1. Verification of the Burgers vector

To confirm the identity of the dislocation, we proceed to find its Burgers vector. Because of the stacking faults two Burgers circuits are needed and we follow exactly the same procedure as before (Cottrell, 1965; Kovacs & Zsoldos, 1973). The resulting Burgers vectors from the two circuits are pointing along $[1\bar{1}\bar{2}]$ and $[\bar{1}12]$ directions, respectively, while their magnitudes correspond to 30° partials' edge components, as in the L–C configuration. The directions of the edges, however, are reversed so that the vectors are pointing away from the core. By subtracting the small circuit's vector from the larger one, a residual vector of $a/3[001]$ is obtained, which indicates a pure-edge and indeed corresponds to the sessile Hirth lock.

5.2. Discussion of the Hirth lock formation

The Hirth lock dislocation structure is the result of a reaction of two 30° Shockley partials residing on different {111} planes. To obtain the obtuse stair-rod configuration with the given Burgers vector in zinc-blende materials, one of the

Figure 3
Image of an isolated 30° partial dislocation with Te core. The 'second 30° partial' of the same b-type is visualized with the dashed line on the {111} plane. Their intersection is assumed to take place at the single Cd–Te dumbbell, which as a result forms a Te$_3$Cd L–C core variant.

Figure 4
(*a*) Atomic resolution HAADF image of a Hirth lock dislocation. The core is circled and associated with two intrinsic stacking faults (dashed). Two Burgers circuits are constructed. The inset shows a temperature-coded zoomed-in core which consists of single Cd and Te atomic columns. (*b*) The pair of partial dislocations bounding intrinsic stacking faults are arranged based on the upper and lower tetrahedra (*a*-/*b*-types). Combination of the two 30° partials along **CD** results in the stair-rod $\alpha'\beta$ Burgers vector connecting the upper and lower left-hand faces. (*c*) Strain map associated with the Hirth dislocation. Two diffuse regions in compression/tension below/above the core, respectively, can be identified.

participating partials must be *a*-type and the second *b*-type. Otherwise, if two 30° partials of the same *a*-type or *b*-type meet along **CD** making an obtuse angle, there will need to be an extrinsic stacking fault associated with the reaction. We consider two 60° dislocations (*B′C* and *CA*), dissociated in their respective glide planes. Fig. 4(*b*) shows initial positions of the pair of extended dislocations associated with intrinsic stacking faults and referring to equations (5) and (6). Leading 30° partials ($\alpha'C$ and $C\beta$) will combine according to equations (7) and (8) along the line of intersection **CD** canceling their screw components and producing new partial dislocation with a pure-edge character.

$$\mathbf{B'C} \rightarrow \mathbf{B'\alpha'} + \mathbf{\alpha'C} \quad (\mathbf{B'CD}), \tag{5}$$

$$\mathbf{CA} \rightarrow \mathbf{C\beta} + \mathbf{\beta A} \quad (\mathbf{ACD}), \tag{6}$$

$$\mathbf{B'C} + \mathbf{CA} \rightarrow \mathbf{B'\alpha'} + \mathbf{\beta A} + (\mathbf{\alpha'C} + \mathbf{C\beta}) \rightarrow \mathbf{B'\alpha'} + \mathbf{\beta A} + \mathbf{\alpha'\beta}, \tag{7}$$

$$a/2[011] + a/2[0\bar{1}1] \rightarrow a/6[\bar{1}12] + a/6[1\bar{1}2] + a/3[001]. \tag{8}$$

The Burgers vector $\mathbf{\alpha'\beta}$ connects the midpoints of the same side upper $B'CD$ and lower ACD faces. The vector can also be expressed as $\mathbf{\alpha\beta}/\mathbf{CD}$ if only the single upper tetrahedron is used (Hirth & Lothe, 1982). Note that the configuration in Fig. 4(*b*) correctly predicts that the Te atomic column within the circled dumbbell-like core in Fig. 4(*a*) will sit right above Cd. This also suggests that no significant rearrangement of the initial 30° partials' core-atom geometries takes place during the reaction. The polar counterpart of the Hirth lock dislocation core, having anti-parallel Burgers vector, will have the same chemical composition. The environments that the intra-core Cd or Te atoms of either variant see, however, would be slightly different and is more apparent with respect to the second and further nearest neighbors. Using Frank's $\mathbf{b}^2$ criteria and comparing $\mathbf{b}^2_{\text{L-C}}$ and $\mathbf{b}^2_{\text{Hirth}}$ it turns out that the L–C product dislocation has lower elastic energy compared to the Hirth lock dislocation by a factor of two. Despite the higher predicted elastic energy, the Hirth core is more compact and consists of only two atomic columns rather than four as in the L–C counterpart.

5.3. Strain-field analysis

Similarly to the strain fields of the L–C dislocation, we do not see any 'hot spots' at the Hirth core and the calculation places most of the compressive/tensile $\varepsilon_{yy}(\mathbf{r})$ distortions on the stacking fault planes (Fig. 4*c*). Shear stresses, not presented here, are likewise narrowly localized to the faulted planes. However, we notice two diffuse regions in $\varepsilon_{yy}(\mathbf{r})$ several ångströms in radius right below and above the core that show lattice compression and tension, respectively. The values within the areas on either side of the core reach ±4%.

6. Conclusions

In summary, we have determined the atomic structure and chemical composition of the two lowest elastic energy polar

stair-rod dislocations in CdTe. By forming double Burgers circuits, as proposed by Cottrell, we confirmed that these are indeed extended Lomer–Cottrell and Hirth lock dislocations. By simple extension of Thompson's tetrahedron, to take into account the polar dislocations, the chemical composition of stair-rod dislocation cores can be effectively predicted. Lomer–Cottrell dislocations can either be Cd rich with Cd_3Te structure or Te rich Te_3Cd. Hirth cores, on the other hand, always consist of a single dumbbell-like Cd–Te atomic column. Despite the higher elastic energy of Hirth dislocation, the core is much more compact and is less likely than L–C to be electrically active. Future first-principles calculations can confirm the proposed atomic arrangement in the core and elucidate the relationship between the core structure and the measured strain fields. From the strain-field analysis, we see that both cores have rather weak and localized associated stresses. Being pure-edge dislocations, the stair-rods can make up the dislocation cores on low-angle tilt-grain boundaries, while the polar L–C-like core arrangement can be found in certain CSL interfaces. The sessile nature of the dislocations may also have an important role in the mechanical behavior of nanometre-scaled semiconductor devices subjected to stresses from fabrication or operation processes.

References

Beckman, S. P., Xu, X., Specht, P., Weber, E. R., Kisielowski, C. & Chrzan, D. C. (2002). *J. Phys. Condens. Matter*, **14**, 12673–12680.

Blumenau, A. T., Jones, R. & Frauenheim, T. (2003). *J. Phys. Condens. Matter*, **15**, S2951–S2960.

Colegrove, E., Banai, R. & Blissett, C. (2012). *J. Electron. Mater.* **41**, 2833–2837.

Cosgriff, E. C., Nellist, P. D., Hirsch, P. B., Zhou, Z. & Cockayne, D. J. H. (2010). *Philos. Mag.* **90**, 4361–4375.

Cottrell, A. H. (1965). *Theory of Crystal Dislocations*. New York: Gordon and Breach.

Egerton, R. F. (1996). *Electron Energy-Loss Spectroscopy in the Electron Microscope*. New York: Plenum Press.

Green, M. A., Emery, K., Hishikawa, Y., Warta, W. & Dunlop, E. D. (2013). *Prog. Photovolt. Res. Appl.* **21**, 1–11.

Hirth, J. P. & Lothe, J. (1982). *Theory of Dislocations*. New York: Wiley.

Hornstra, J. (1958). *J. Phys. Chem. Solids*, **5**, 129–141.

Hÿtch, M. J. & Plamann, T. (2001). *Ultramicroscopy*, **87**, 199–212.

Hÿtch, M., Snoeck, E. & Kilaas, R. (1998). *Ultramicroscopy*, **74**, 131–146.

Kovacs, I. & Zsoldos, L. (1973). *Dislocations and Plastic Deformation*. Oxford: Pergamon Press.

Li, C., Poplawsky, J., Wu, Y., Lupini, A. R., Mouti, A., Leonard, D. N., Paudel, N., Jones, K., Yin, W., Al-Jassim, M., Yan, Y. & Pennycook, S. J. (2013). *Ultramicroscopy*, **134**, 113–125.

Li, C., Wu, Y., Pennycook, T. J., Lupini, A. R., Leonard, D. N., Yin, W., Paudel, N., Al-Jassim, M., Yan, Y. & Pennycook, S. J. (2013). *Phys. Rev. Lett.* **111**, 096403.

Li, C., Wu, Y., Poplawsky, J., Pennycook, T. J., Paudel, N., Yin, W., Haigh, S. J., Oxley, M. P., Lupini, A. R., Al-Jassim, M., Pennycook, S. J. & Yan, Y. (2014). *Phys. Rev. Lett.* **112**, 156103.

Louchet, F. & Thibault-Desseaux, J. (1987). *Rev. Phys. Appl.* **22**, 207–219.

Mahajan, S. (2000). *Acta Mater.* **48**, 137–149.

Nunes, R. W., Assali, L. V. & Justo, J. F. (2004). *Comput. Mater. Sci.* **30**, 67–72.

Phillips, P. J., Paulauskas, T., Rowlands, N., Low, K. B., Nicholls, A. W., Bhadare, S. & Klie, R. F. (2014). *Microsc. Microanal.* **20**, 1046–1052.

Shockley, W. & Queisser, H. J. (1961). *J. Appl. Phys.* **32**, 510.

Sutton, A. P. & Balluffi, R. W. (1995). *Interfaces in Crystalline Materials*. New York: Oxford Science Publications.

Takeuchi, S. & Suzuki, K. (1999). *Phys. Status Solidi*, **171**, 99–103.

Thompson, N. (1953). *Proc. Phys. Soc. B*, **66**, 481.

Yan, Y., Al-Jassim, M. M. & Jones, K. M. (2003). *J. Appl. Phys.* **94**, 2976.

Zhu, Y., Ophus, C., Ciston, J. & Wang, H. (2013). *Acta Mater.* **61**, 5646–5663.